Automatic Vessel Segmentation from Pulsatile Radial Distension

Alborz Amir-Khalili[1], Ghassan Hamarneh[2], and Rafeef Abugharbieh[1]

[1] BiSICL, University of British Columbia, Vancouver, Canada
[2] Medical Image Analysis Lab, Simon Fraser University, Burnaby, Canada

Abstract. Identification of vascular structures from medical images is integral to many clinical procedures. Most vessel segmentation techniques ignore the characteristic pulsatile motion of vessels in that formulation. In a recent effort to automatically segment vessels that are hidden under fat, we motivated the use of the magnitude of local pulsatile motion extracted from surgical endoscopic video. In this paper we propose a new approach that leverages the local orientation, in addition to magnitude of motion, and demonstrate that the extended computation of motion vectors can improve the segmentation of vascular structures. We implement our approach using two alternatives to magnitude-only motion estimation by using traditional optical flow and by exploiting the monogenic signal for fast flow estimation. Our evaluations was conducted on both synthetic phantoms as well as real ultrasound data showing improved segmentation results (325% increase in DSC and 13% increase in AUC) with negligible change in computational performance.

1 Introduction

Identification of blood vessels from medical images is important to many clinical procedures. Extraction of vascular structures are of such importance that many acquisition techniques and imaging modalities have been developed to image vasculature. Such techniques include contrast enhanced computed tomography (CT) or magnetic resonance (MR) angiography, laser speckle imaging [1], color Doppler ultrasound (US) and optical coherence tomography (OCT) [2].

Attempts have been made to automatically extract, or segment, these structures by applying advanced image analysis techniques to the intensity information acquired from the aforementioned modalities. Such attempts include the exploitation of ridge-like features in the image [3], a combination of wavelet-based features and machine learning [4], Hessian-based vesselness features [5,6], model/physics based approaches [7,6], active contours [8], and supervised machine learning techniques [9]. With the exception of Doppler US and OCT, the listed techniques focus on extracting features from static information, ignoring the most characteristic feature of a pulsating vessel, i.e. its temporal behavior.

US and OCT are capable of measuring the directionality and relative velocity of structures (usually blood) by leveraging the Doppler effect. The flow of blood,

however, is not the only temporal characteristic of vascular structures. The pulsatile radial distension of the vascular walls (from the lumen to tunica externa) is another characteristic that can be observed and measured using almost any imaging modality so long as the temporal and spatial resolutions are adequate.

Recently, we demonstrated in [10] that phased-based (PB) Eulerian techniques can be used to detect the motion of renal vessels at a sub-pixel level by analyzing the temporal change in phase. Our early work did not explicitly compute the deformation vectors (magnitude and orientation) of structures in the image through time. The estimation of said vectors is computationally expensive and thus not appropriate in the context of robotic surgery. In this contribution, we propose that 1) a more detailed computation of motion characteristics (i.e. an estimation of the *local orientation* of motion) can increase the accuracy of motion based vessel segmentation, and 2) by reconstructing the monogenic signal (MON) [11], the local orientation of motion may be estimated concurrently while increasing the computational performance of the method.

We propose a robust vessel segmentation technique that models local motion of vessels subject to pulsatile radial distension. We estimate all components of motion using traditional optical flow (OF) and faster MON based flow estimation [12]. This complete representation of motion allows us to analyze the local orientation of motion to remove outliers on objects that are undergoing mere translational motion while amplifying the response of structures that behave like a truly pulsating vessel, i.e., periodically expand and contract in time. Using computational phantoms, we evaluate the performance of our motion estimation methods while comparing it to our old PB method [10]. Finally. we validate our segmentations on US images acquired from human volunteers.

2 Methods

Our method relies on a complete estimation of motion. Optical flow methods, such as the one proposed by Sun et al. [13], compute apparent local motions of objects in a sequence of images by imposing the brightness consistency assumption. Similarly, the MON signal may be used to estimate this local motion more efficiently. The MON signal is a 2D extension of the analytic signal and it provides a framework for extracting the local orientation θ and the local phase ϕ features from an image. By measuring the temporal change in θ and ϕ in a sequence of images, we can estimate motion [12]. In this paper, each j^{th} frame of such sequence is defined as a scalar valued (grayscale) function $f_j : \mathbf{x} \subset \mathbb{R}^2 \rightarrow \mathbb{R}$ mapping a pixel $\mathbf{x} = (x_1, x_2)^\intercal$ in the spatial domain to an intensity value. The MON signal is constructed from a trio of bandpass filters with finite spatial support. This trio is called a spherical quadrature filter (SQF) [11]. To estimate the motion of both small and large structures in each frame, we generate different SQFs by tuning the spatial passband of the filters to varying scales. We first provide a brief summary of the SQFs used and how we estimate local motion vectors from the MON signal of a sequence of frames. Lastly, we explain how local motion extracted using MON or OF is used to identify pulsating structures.

The Monogenic Framework: Each SQF is comprised of an even (symmetric) radial bandpass filter and two odd (antisymmetric) filters. The odd filters are computed from the Riesz transform, a 2D generalization of the Hilbert transform, of the radial bandpass filter [11]. We employ Log-Gabor bandpass filters as they suit the natural statistics of an image [4,14] and maintain zero DC gain at lower spatial scales. For every scale s, the even component of the SQF is expressed as

$$B_e(\mathbf{u}; s) = \exp\left(\frac{-\left[\log\left(|\mathbf{u}|/\omega_s\right)\right]^2}{2\left[\log k\right]^2}\right), \tag{1}$$

in the frequency domain $\mathbf{u} = (u_1, u_2)^\intercal$, where k and ω_s are parameters of the filter. The parameter $k = \sigma/\omega_s$ is a fixed constant representing the ratio of the standard deviation σ of the Gaussian describing the Log-Gabor filter's transfer function in the frequency domain to the filter's center frequency ω_s. At each scale s, the center frequency is defined as $\omega_s = (\lambda_0 2^{(s-1)})^{-1}$, where λ_0 is an initial minimum wavelength. Note that B_e is symmetric as it is only a function of the magnitude of the frequency $\mathbf{u}$. Using the Riesz transform, we compute the two odd components (B_{o1} and B_{o2}) associated to this SQF as

$$B_{o1}(\mathbf{u}; s) = i\frac{u_1}{|\mathbf{u}|}B_e; \quad B_{o2}(\mathbf{u}; s) = i\frac{u_2}{|\mathbf{u}|}B_e. \tag{2}$$

In the spatial domain, the components of the MON signal $(h_{j,e}, \mathbf{h}_{j,o})$ are obtained by convolving the SQF with a given frame of the sequence such that

$$\begin{aligned} h_{j,e}(\mathbf{x}; s) &= \mathcal{F}^{-1}\left[B_e(\mathbf{u}; s)F_j(\mathbf{u})\right] \\ h_{j,o1}(\mathbf{x}; s) &= \mathcal{F}^{-1}\left[B_{o1}(\mathbf{u}; s)F_j(\mathbf{u})\right] \\ h_{j,o2}(\mathbf{x}; s) &= \mathcal{F}^{-1}\left[B_{o2}(\mathbf{u}; s)F_j(\mathbf{u})\right] \\ \mathbf{h}_{j,o}(\mathbf{x}, s) &= (h_{j,o1}(\mathbf{x}; s), h_{j,o2}(\mathbf{x}; s))^\intercal, \end{aligned} \tag{3}$$

where $F_j(\mathbf{u}) = \mathcal{F}[f_j(\mathbf{x})]$ is the frequency domain representation of the frame.

Extraction of Local Motion from the Local Phase Vector: Let $\mathbf{r}$ be the phase vector, the continuous representation of local orientation θ and local phase information ϕ, which can be computed from (3) such that

$$\mathbf{r}_j(\mathbf{x}; s) = \phi(\cos\theta, \sin\theta)^\intercal = \frac{\mathbf{h}_{j,o}}{|\mathbf{h}_{j,o}|}\arg\left(h_{j,e} + i|\mathbf{h}_{j,o}|\right). \tag{4}$$

Local motion may then be calculated by first computing the components of a 3D rotation that relates the response of two adjacent frames in the video

$$\begin{aligned} h_{\text{diff},e} &= h_{j,e}h_{j+1,e} + \mathbf{h}_{j,o}^\intercal\mathbf{h}_{j+1,o} \\ \mathbf{h}_{\text{diff},o} &= h_{j,e}\mathbf{h}_{j+1,o} - h_{j+1,e}\mathbf{h}_{j,o} \end{aligned} \tag{5}$$

and then computing the phase differences $\mathbf{r}_{\text{diff}}$ by solving (4) using (5). Given a local neighborhood $\mathcal{N}$, the local displacement $\mathbf{d}_{\mathcal{N}}$ is calculated from

$$\sum_{\mathbf{x}\in\mathcal{N}}\left[\nabla^\intercal\mathbf{r}_j(\mathbf{x}; s)\right]\mathbf{d}_{\mathcal{N},j} = \sum_{\mathbf{x}\in\mathcal{N}}\mathbf{r}_{\text{diff}}(\mathbf{x}; s) \tag{6}$$

Fig. 1: Overview of the motion based vessel segmentation pipelines.

where $\nabla^\intercal$ is the divergence operator. The derivation of (4), (5), and (6) from the response to the SQF is outside the scope of this paper and can be found in [12]. To improve the estimate for the displacement vector $\mathbf{d}_{\mathcal{N},j}$, we compute the mean of this value across all scales s. The computed $\mathbf{d}_{\mathcal{N},j}$ is an estimate of the true motion vectors $\mathbf{d}_j(\mathbf{x})$ that relates two frames in a sequence $f_{j+1}(\mathbf{x}) = f_j(\mathbf{x} - \mathbf{d}_j(\mathbf{x}))$. This is the same motion vector that is computed by traditional OF techniques.

Modeling of Radial Distension: Let $\mathbf{d}(\mathbf{x}, j)$ define motion field containing the motion vectors estimated for all adjacent fames inside a given sequence. We first isolate the motions that are in sync with the heart rate by applying the same ideal temporal bandpass filter (Fig. 1) used in [10] to each location in $\mathbf{x}$ of the motion vector $\mathbf{d}(\mathbf{x}, j)$ independently. Let h be the temporal filter defined as

$$h(\mathbf{x}, j) = 2b_H \mathtt{sinc}(2b_H j) - 2b_L \mathtt{sinc}(2b_L j), \tag{7}$$

where b_L is the low frequency cutoff and b_H is the high frequency cutoff. We define the temporally bandpassed motion vectors as $\hat{\mathbf{d}}(\mathbf{x}, j) = \mathbf{d}(\mathbf{x}, j) * h(\mathbf{x}, j)$.

Temporal filtering alone does not distinguish between structures that distend radially and tissues that translate at pulsatile frequency. Pulsating vessels are subject to periodic expansion and contraction, which implies that the orientation of the motion vectors are opposing each other along the centerline of the vessel. Such vector fields thus exhibit high *divergence* along the centerline.

Due of the tubular geometry of vessels, the radial motion along the centerline of the vessels are weaker compared to the regions that are along the walls. We account for this by computing the divergence across multiple spatial scales; the motion field at each scale denoted $\hat{\mathbf{d}}(\mathbf{x}, j; s)$. At each scale, we downsample the vector field by a factor of two using bilinear interpolation. Our resulting vessel labels are computed to be

$$I(\mathbf{x}) = \frac{1}{M} \sum_{\forall j} \sum_{\forall s} |\nabla^\intercal \hat{\mathbf{d}}(\mathbf{x}, j; s)|, \tag{8}$$

where M is a normalizing factor to fix the range of I to [0 1].

3 Results and Discussion

In this section we present two experiments to evaluate the performance of our method against the state-of-the-art. In the experiments, we compare our proposed MON and OF pipelines with the PB method (Fig. 1).

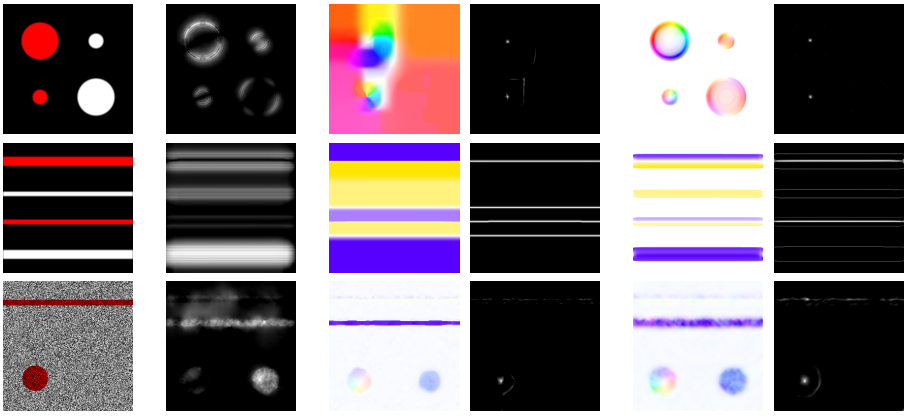

(a) Phantom (b) PB Seg. (c) OF (d) OF Seg. (e) MON (f) MON Seg.

Fig. 2: Qualitative phantom experiments showing segmentation results of PB and our vessel extraction applied to OF and MON. All resulting segmentations were thresholded at 0.3 for visibility. Fuzzy segmentations of our method depict high (white) response at the center of the pulsating structures. Top row: phantom with circular shapes of varying sizes. Middle row: tubular shapes of varying sizes. Bottom row: A randomly generated texture subjected to local deformations that include a combination of translating/pulsating circular/tubular structures. Column (a): the first image of the phantom with red overlay indicating structures that distend radially, the other structures are subject to translation only. Column (c & e): the color encoding of the motion vectors extracted using OF and MON respectively.

Materials and Experimental Setup: For the real data experiments, we use eight US sequences of the common carotid artery (CCA) acquired from three volunteers. Although our methods are applicable to other imaging modalities, US is ideal for validation as it can image vessels in the transverse and longitudinal axes, it has high temporal resolution, and the vessels can be manually delineated with accuracy for evaluation against ground truth. The first frame of each sequence was segmented manually for quantitative analysis. All of the computational phantoms and the methods described were implemented in MATLAB 2011b running on a workstation with two Intel 3GHz Xeon x5472 processors and 8GB of RAM. We use the MATLAB code and default parameters of PB [10] and the `classic+nl-fast` setting of OF [13]. For the MON method, the minimum wavelength λ_0 is set to 2, ratio k was set to 0.05, and a 7×7 square filter was used to average the displacements over the neighborhood of $\mathcal{N}$. The number of scales are set such that $s = \lfloor \log_2(L) \rfloor - 1$ where L is the smallest image dimension.

Phantom Experiment: We use three computational phantoms, in a two-frame matching experiment, to compare the effectiveness of our proposed MON and OF based segmentation techniques to the PB method. Temporal filtering was not

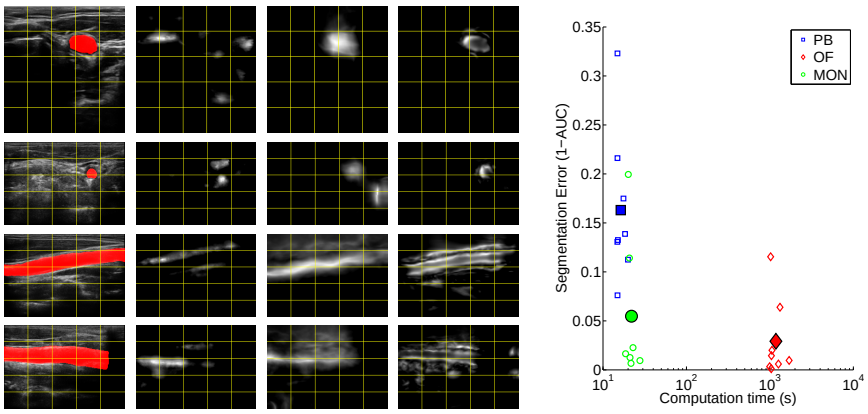

(a) US (b) PB Seg. (c) OF Seg. (d) MON Seg. (e)

Fig. 3: Experiment with real data. Exemplar US image of CCA in axial and longitudinal axes. The corresponding US ground truth for the vessel is shown in red. Yellow gridlines are superimpsoed to enhance correspondence. All resulting segmentations were thresholded at 0.3 for visibility. (e) Performance of each segmentation method, corresponding averages illustrated with filled markers and black outline.

used in this experiment. We constructed three computational phantoms containing: Pulsating and translating circles (top row in Fig. 2), pulsating and translating tubular structures (middle row in Fig. 2), and a noise pattern that undergoes a combination of pulsating and translating motions in the shapes of circles and tubes (bottom row in Fig. 2). The OF flow estimation code used relies heavily on regularization in regions that do not contain salient textures (Fig. 2c). We thus used the third phantom to perform further quantitative comparison between the OF and MON flow estimation modules. We computed the error in flow endpoint to the ground truth $\mathbf{d}_{GT}$ defined as $\|\mathbf{d}-\mathbf{d}_{GT}\|_2$ and observed only a small increase in the mean error from 0.21 pixels (OF) to 0.28 (MON).

Real Data Experiment: Real data evaluation was done on eight US sequences of the CCA along the transverse and longitudinal axes, where the vessel appears as a pulsating ellipsoid and tube respectively. The passband of the temporal filter was tuned depending on the patient's approximate heart rate, denoted b_r. The parameters were set such that $b_L = b_r/2$ and $b_H = 2b_r$. Four exemplar cases of our fuzzy segmentation labels are shown in Fig. 3. To clarify the advantages to each approach as a trade-off between accuracy and computation time, we present quantitative analysis (Fig 3e) using the ground truth segmentations of the US sequences. We report the area under the receiver operating characteristics curve (AUC) for each case (thresholding the fuzzy segmentations from 0 to 1) as a measure of segmentation accuracy, in which the value of 1 indicates perfect segmentation and 0.5 is the noise threshold.

Discussions: From our analysis, we conclude that the MON approach is the best candidate for segmenting vasculature from pulsatile motion. Fig. 3e shows that the MON method can, on average, achieve comparable accuracy with OF method while maintaining similar performance as the PB method. The comparable performance of MON vs OF flow estimation is further confirmed by the analysis of the endpoint errors. Compared to PB (Fig 3b), with the addition of our proposed orientation based vessel segmentation, our MON (Fig 3d) and OF (Fig 3c) pipelines are more specific to motion of the CCA. In Fig. 3b, the false positives that occur on the surrounding soft tissues have been reduced.

Quantitatively, the average AUC was increased from 0.84 (PB) to 0.97 (OF) and 0.95 (MON). Binarizing the segmentations at 0.5 yields a significant increase in average Dice similarity coefficient (DSC) from 0.16 (PB) to 0.55 (OF) and 0.52 (MON). The average run times for the 40 frame US sequences (without distension modeling) are: 16 s for PB, 19.6 min for OF, and 15 s for the MON method; the modeling step costs an additional 7 s for OF and MON. Our unoptimized MATLAB implementation of MON is drastically faster than OF and slightly faster than the PB method. We predict that the MON method has the potential to further outperform the PB method, as our SQF is composed of three filters per scale whereas the PB method uses a total of eight filters per scale.

In the domain of US image processing, SQFs have been shown to improve the extraction of structures, during radio frequency (RF) signal to B-mode conversion, by demodulating the RF in a 2D context [15]. This implies that our method may be used to extract local motion information from raw RF data, allowing for direct implementation in a native representation of acquired data.

Our Eulerian approach is not yet able to cope with gross out-of-plane motion, common during 2D US acquisitions, because our current implementation of the MON framework is in two spatial dimensions. As noted in [16], the steerable approach of Portilla and Simoncelli [17] that was used in the PB method is hard to transpose into 3D due to its invertibility. The MON formulation can however be extended to 3D [16]. This will allow our proposed method to be extended to volumetric images such as 3D CT fluoroscopy, Cine MRI, and 3D US.

4 Conclusions

We presented evidence that more robust and faster automatic segmentation of vasculature is achievable by analyzing the characteristic pulsatile radial distension of vascular structures. Specifically we have shown that 1) the local orientation of motion extracted from a sequence can be used to highlight the center of a pulsating vessel where the *divergence* of the motion vector field is high, and 2) the MON framework is capable of estimating the amplitude *and* orientation of local motion faster than the PB method. Using US sequences acquired from the CCA, we have shown that the performance of the PB method can be increased from an average AUC of 0.84 to 0.95 while slightly increasing the computation time from 15 to 22 seconds. The proposed MON method can be optimized fur-

ther through the precomputation of the SQFs, may be applied to native RF data, and can be extended to process volumetric (3D+time) data.

References

1. Murari, K., Li, N., Rege, A., Jia, X., et al.: Contrast-enhanced imaging of cerebral vasculature with laser speckle. Applied Optics **46**(22) (2007) 5340–5346
2. Izatt, J.A., Kulkarni, M.D., Yazdanfar, S., Barton, J.K., Welch, A.J.: In vivo bidirectional color doppler flow imaging of picoliter blood volumes using optical coherence tomography. Optics letters **22**(18) (1997) 1439–1441
3. Staal, J., Abràmoff, M.D., Niemeijer, M., Viergever, M.A., van Ginneken, B.: Ridge-based vessel segmentation in color images of the retina. Transactions on Medical Imaging **23**(4) (2004) 501–509
4. Soares, J.V., Leandro, J.J., Cesar, R.M., Jelinek, H.F., Cree, M.J.: Retinal vessel segmentation using the 2-D Gabor wavelet and supervised classification. Transactions on Medical Imaging **25**(9) (2006) 1214–1222
5. Frangi, A.F., Niessen, W.J., Vincken, K.L., Viergever, M.A.: Multiscale vessel enhancement filtering. In: Medical Image Computing and Computer-Assisted Intervention. (1998) 130–137
6. Hennersperger, C., Baust, M., Waelkens, P., Karamalis, A., Ahmadi, S., Navab, N.: Multiscale tubular structure detection in ultrasound imaging. Transactions on Medical Imaging **34**(1) (2015) 13–26
7. Vermeer, K.A., Vos, F.M., Lemij, H., Vossepoel, A.M.: A model based method for retinal blood vessel detection. Computers in Biology and Medicine **34**(3) (2004) 209–219
8. Lorigo, L.M., Faugeras, O.D., Grimson, W.E.L., Keriven, R., Kikinis, R., Nabavi, A., Westin, C.F.: Curves: Curve evolution for vessel segmentation. Medical Image Analysis **5**(3) (2001) 195–206
9. Becker, C., Rigamonti, R., Lepetit, V., Fua, P.: Supervised feature learning for curvilinear structure segmentation. In: Medical Image Computing and Computer-Assisted Intervention. (2013) 526–533
10. Amir-Khalili, A., Hamarneh, G., Peyrat, J.M., Abinahed, J., Al-Alao, O., Al-Ansari, A., Abugharbieh, R.: Automatic segmentation of occluded vasculature via pulsatile motion analysis in endoscopic robot-assisted partial nephrectomy video. Medical Image Analysis (2015)
11. Felsberg, M., Sommer, G.: The monogenic signal. Transactions on Signal Processing **49**(12) (2001) 3136–3144
12. Felsberg, M.: Optical flow estimation from monogenic phase. In: Complex Motion. (2007) 1–13
13. Sun, D., Roth, S., Black, M.J.: Secrets of optical flow estimation and their principles. In: Computer Vision and Pattern Recognition, IEEE (2010) 2432–2439
14. Field, D.J.: Relations between the statistics of natural images and the response properties of cortical cells. JOSA A **4**(12) (1987) 2379–2394
15. Wachinger, C., Klein, T., Navab, N.: The 2D analytic signal on RF and B-mode ultrasound images. In: Information Processing in Medical Imaging. (2011) 359–370
16. Chenouard, N., Unser, M.: 3D steerable wavelets and monogenic analysis for bioimaging. In: International Symposium on Biomedical Imaging, IEEE (2011) 2132–2135
17. Portilla, J., Simoncelli, E.P.: A parametric texture model based on joint statistics of complex wavelet coefficients. IJCV **40**(1) (2000) 49–70